4-28-94
E8702

Computational Study of Single-Expansion-Ramp Nozzles With External Burning

Shaye Yungster
Institute for Computational Mechanics in Propulsion
Lewis Research Center
Cleveland, Ohio

and

Charles J. Trefny
Lewis Research Center
Cleveland, Ohio

National Aeronautics and
Space Administration

Computational Study of Single-Expansion-Ramp Nozzles With External Burning

Shaye Yungster
Institute for Computational Mechanics in Propulsion
NASA Lewis Research Center, Cleveland, OH 44135
and
Charles J. Trefny
NASA Lewis Research Center, Cleveland, OH 44135

Abstract

A computational investigation of the effects of external burning on the performance of single expansion ramp nozzles (SERN) operating at transonic speeds is presented. The study focuses on the effects of external heat addition and introduces a simplified injection and mixing model based on a control volume analysis. This simplified model permits parametric and scaling studies that would have been impossible to conduct with a detailed CFD analysis. The CFD model is validated by comparing the computed pressure distribution and thrust forces, for several nozzle configurations, with experimental data. Specific Impulse calculations are also presented which indicate that external burning performance can be superior to other methods of thrust augmentation at transonic speeds. The effects of injection fuel pressure and nozzle pressure ratio on the performance of SERN nozzles with external burning are described. The results show trends similar to those reported in the experimental study, and provide additional information that complements the experimental data, improving our understanding of external burning flowfields. A study of the effect of scale is also presented. The results indicate that combustion kinetics do not make the flowfield sensitive to scale.

Introduction

The possibility of achieving orbital conditions with a single-stage vehicle using primarily airbreathing propulsion is being evaluated under the National Aerospace Plane program. Ready access to space, a reduction in the cost of putting payloads into orbit, and very high

speed earth transportation are some of the benefits of this technology. The propulsion system of such a vehicle will have to cover the total flight spectrum from horizontal takeoff to orbital speed. Efficient operation at high Mach numbers dictates the use of hydrogen as the fuel of choice, and a highly integrated vehicle design. An artist's conception of a single-stage to orbit "Aerospace Plane" is shown in Fig. 1. The entire aft end of the vehicle acts as a single expansion ramp nozzle, providing a very high area ratio which is exploited at the high nozzle pressure ratios associated with high Mach number and altitude. Such a vehicle, however, will presumably not incorporate variable geometry in order to minimize the structural weight. Therefore, the large aft-facing area becomes a great liability at transonic and low supersonic speeds where low airbreathing engine pressure ratios result in a highly over-expanded nozzle.

Figure 2 illustrates a single expansion ramp nozzle operating at transonic speeds. The exhaust mass flow is insufficient to fill the large area-ratio nozzle designed for high Mach number operation. The shear layer and shock wave system adjust and stabilize in a configuration that equalizes the pressure in the nozzle plume and external flow. Due to the freestream flow turning around the aerodynamic shape formed by the cowl and the shear layer, the resulting pressure acting on the nozzle expansion surface is below atmospheric pressure, resulting in low thrust levels.

An effective method for improving nozzle performance at transonic speeds is based on the concept of external burning. Fuel, in this case hydrogen, is injected into the external flow and is subsequently mixed and burned (Fig. 3), pressurizing the entire expansion surface and cowl trailing edge.

The external burning concept described above depends on the controlled combustion of hydrogen and air at freestream conditions. Experimental studies aimed at determining the effects of hydrogen-air external burning

1

on the performance of SERN nozzles were reported in Refs. [1] and [2]. These studies indicated the potential for specific impulse values in excess of other auxiliary propulsion options such as turbomachinery and rockets.

The objectives of the present work are to develop CFD prediction techniques to analyze the sub-scale and full-scale performance of external burning nozzles at transonic flight conditions; and to understand how the various parameters (such as fuel injection pressure, nozzle pressure ratio, Mach number, etc) affect the performance of the external burning system. In the following sections, we describe first the computational model used, the governing equations and numerical method employed. Then, several model validation tests are presented followed by parametric and scaling studies of several nozzle configurations.

Computational Model

A detailed analysis of the entire external burning flow-field would be extremely demanding computationally. Such a task must address the details of fuel injection and flameholding, mixing, turbulent boundary layers and shear layers, reaction kinetics and their interaction with the turbulent flowfield. Furthermore, the external burning process creates a large subsonic region that requires a computational domain that extends far beyond the expansion ramp. The requirement of an extended domain, combined with the need to resolve the various detailed flow features would result in a very large computational grid. The use of finite rate chemistry combined perhaps with a probability density function (PDF) model for proper treatment of the chemistry-turbulence interaction would lead to prohibitively expensive CPU times.

Previous studies of external burning have been based on simplified analytical models, or "engineering" type CFD approaches in order to determine trends and provide insight into the various complex phenomena occurring in this type of flow. An overview of past analytical methods to investigate external burning flowfields was presented in Ref. [1].

CFD studies have focused on certain aspects of the flowfield. Bittner and McClinton [3] used 2D, 3D, and PNS versions of the SPARK code to study the injection, ignition and flameholding characteristics of external burning flows. Their study was based on a simplified geometry and did not analyze the overall effects of external burning on the nozzle performance. Trefny [1] on the other hand, ignored the details of the injection and mixing processes to investigate drag reduction by external burning on an expansion surface. The injection and mixing in Trefny's study were modeled as a stream-tube of premixed hydrogen-air, and an external heat addition term was retained in the energy equation.

The present investigation follows an approach similar to that of Ref. [1] but includes a more elaborate flow model, and considers the actual nozzle configurations studied experimentally in Ref. [2]. The focus is on the global effect of external heat addition on nozzle performance, without modeling in detail the injection process. Therefore, in the present work, the injection and mixing are modeled as a stream-tube of premixed hydrogen-air (Fig. 4).

A second simplification used in this work is related to the three-dimensional nature of the flowfield. SERN nozzles operating at transonic speeds without external burning are characterized by strong three-dimensional effects. The low pressure in the nozzle plume gives rise to a transverse flow from the surrounding higher pressure air. When external burning is used, however, the net effect is to pressurize the nozzle plume and external flow to atmospheric levels or higher. As a result, the three-dimensional relieving effect is much weaker. Therefore, it is reasonable to assume that SERN nozzles that include external burning can be adequately modeled using a 2D formulation.

Injection and Mixing Model

The external burning fuel injection configuration considered here is the same as that used in the experimental studies of Refs. [1] and [2]. A single row of normal fuel injectors was located along the external cowl surface, as shown schematically in Fig. 5. The fuel injection scheme consisted of 21 choked orifices, each $d = 0.060$ inches in diameter with a spacing $s = 0.381$ inches apart, resulting in a spacing ratio $s/d = 6.35$.

In the present work, the injection process is modeled as a uniform stream-tube of premixed hydrogen-air. The performance of external burning is theoretically a function of the equivalence ratio of this fueled stream. This external burning equivalence ratio cannot be practically measured and will not be uniform for some distance following the normal injection of fuel. Therefore, a method of estimating a "global" equivalence ratio needs to be devised. This is done based on a jet penetration correlation and a control volume analysis around a single hydrogen injector.

The jet penetration height, y_p, is determined from the correlation developed by Povinelli [4], which gives an equation that describes the outer boundary of the injectant, defined as a 0.5% concentration by volume. For sonic orifices this correlation is given by

$$\frac{y_p}{d} = 1.12 \left(\frac{p_{t,f}}{p_{eff}}\right)^{.483} \left(\frac{\tilde{x}}{d} + 0.5\right)^{.281} \tag{1}$$

$$p_{eff} = \frac{2}{3} p_{t,NS} \tag{2}$$

where $p_{t,f}$ is the fuel injector total pressure, p_{eff} is an effective back pressure taken to be 2/3 of the stagnation

pressure behind a normal shock, $p_{t,NS}$, at the freestream Mach number. The parameter $\tilde{x}$ denotes the distance downstream of the orifice centerline. This distance is a free parameter for which an appropriate value must be chosen. For $\tilde{x}/d$ greater than about 20, the jet penetration is a relatively weak function of $\tilde{x}/d$ because of its .281 exponent. An $\tilde{x}/d$ of 30 was therefore chosen for all subsequent calculations [1].

Once the jet penetration has been estimated, the properties of the hydrogen-air stream-tube can be computed using a control volume analysis. Figure 5 shows a control volume around a single fuel injector. The central assumptions used in the analysis are: 1) the flow coming out of the exit area A_e has a uniform composition; and 2) the height of the hydrogen-air stream-tube exiting the control volume is equal to the jet penetration y_p. Therefore the exit area A_e is given by

$$A_e = y_p s \tag{3}$$

where s is the spacing between the orifices. Thus each orifice fuels a stream-tube of air of cross-section A_i. The capture area A_i remains to be determined.

Considering the control volume delimited by the cowl surface and the mixing boundary streamline, conservation of mass gives

$$\dot{m}_a + \dot{m}_f = \dot{m}_e \tag{4}$$

where

$$\dot{m}_a = \rho_a u_a A_i \tag{5}$$

$$\dot{m}_e = \rho_e u_e A_e \tag{6}$$

where ρ_a and u_a are the density and velocity of the incoming air respectively. Similarly, ρ_e and u_e denote the density and velocity of the mixture exiting through A_e. The parameter $\dot{m}_f$ denotes the fuel mass flow rate. Now, considering conservation of mass for the whole control volume having inflow and exit area A

$$\dot{m}_e + \rho_a u_a (A - A_e) + \dot{m}_s - \dot{m}_f - \rho_a u_a A = 0 \tag{7}$$

where $\dot{m}_s$ is the mass flow of air through the side of the control volume. Rearranging, and using Eq (4) we obtain

$$\dot{m}_s = \rho_a u_a (A_e - A_i) \tag{8}$$

Conservation of momentum, assuming that no net thrust is produced by the fuel injection process, can be written as

$$
\begin{aligned}
(p_a - p_e)A_e &= \dot{m}_e u_e + \dot{m}_s u_a + \rho_a u_a (A - A_e) u_a - \\
&\quad \dot{m}_a u_a - \rho_a u_a (A - A_i) u_a
\end{aligned} \tag{9}
$$

using Eq (8) we obtain

$$(p_a - p_e)A_e = \dot{m}_e u_e - \dot{m}_a u_a \tag{10}$$

Assuming that the fueled stream-tube exit pressure, p_e is equal to the air pressure, $p_e = p_a$, and defining the fuel-air ratio $f = \dot{m}_f / \dot{m}_a$ we have

$$u_e = \frac{u_a}{(1+f)} \tag{11}$$

Eqs. (4) and (6) can then be written as

$$\frac{\dot{m}_f}{A_e} + \frac{\dot{m}_a}{A_i}\left(\frac{A_i}{A_e}\right) = \frac{\dot{m}_e}{A_e} \tag{12}$$

$$\frac{\dot{m}_e}{A_e} = \rho_e u_e = \frac{p_e W_e}{R T_e} \frac{u_a}{1+f} \tag{13}$$

where T is the temperature, and W the molecular weight. We will also assume that the fueled stream-tube exit temperature, T_e is equal to the air temperature $T_e = T_a$. The fuel-air ratio can be written

$$f = \frac{\frac{\dot{m}_f}{A_e}}{\frac{\dot{m}_a}{A_i}\left(\frac{A_i}{A_e}\right)} \tag{14}$$

Finally, we obtain the following equation for the capture area ratio A_i/A_e

$$\frac{\dot{m}_e}{A_e} + \frac{\dot{m}_a}{A_i}\left(\frac{A_i}{A_e}\right) = \frac{p_a W_e}{R T_a}\frac{u_a}{1+f} \tag{15}$$

The molecular weight of the fueled stream-tube, W_e, is a function of the fuel-air ratio which in turn depends on the capture area ratio through Eq (14). Equation (15) is solved graphically for A_i/A_e as shown in Fig 6. The left-hand side of Eq (15) is denoted by $\dot{m}_{in}$ and the right-hand side by $\dot{m}_{out}$. The left-and right-hand sides of Eq. (15) are evaluated for several assumed values of A_i/A_e and plotted. The crossover pont represents the solution. The capture area ratio decreases with increasing fuel pressure. In the present stdy, its value was in the range $0.5 < A_i/A_e < 0.9$. Once the capture area ratio is known, the fuel-air ratio is obtained from Eq (14), and the global equivalence ratio, ϕ, of the fueled stream-tube is obtained from the following equation (valid for hydrogen fuel only)

$$\phi = 34.4704 f \tag{16}$$

The following relations are also used

$$\frac{\dot{m}_e}{A_e} = 0.1403 C_v \frac{p_{t,f}}{\sqrt{T_{t,f}}} \frac{\pi d^2}{4 y_p s} \tag{17}$$

and

$$\frac{\dot{m}_a}{A_i} = 0.532 \frac{p_t}{\sqrt{T_t}}\left(\frac{A^*}{A}\right) \tag{18}$$

where C_v is the orifice flow coefficient, $T_{t,f}$ is the fuel injector total temperature, and p_t and T_t are the freestream total pressure and temperature respectively. A^* is the

3

sonic area, and the ratio A^*/A is a function only of the freestream Mach number. In Eqs. (17) and (18), the pressure is in psi, and the temperature is in degrees Rankine.

Code Description

The computational study of SERN nozzles with external burning was carried out using an in-house developed two-dimensional CFD code [5]. As mentioned in the introduction, a two-dimensional approach is adequate for this type of problem. This code solves the multi-species Reynolds-Averaged Navier-Stokes equations with finite-rate chemistry. It is a multiblock, fully implicit finite difference code based on the LU-SSOR factorization scheme. The spatial discretization is based on the second order total variation diminishing (TVD) scheme developed by Yee [6]. In the present study, a symmetric TVD scheme with a minmod type limiter was used. A detailed description of the code can be found in Yungster [5].

The analysis of SERN nozzles that do not include external burning was carried out using a three-dimensional code called MAWLUS, developed by Chitsomboon [7]. Some salient features of MAWLUS are: finite volume, fully implicit, LU factorization, central differencing, and multi-block methodology. Artificial viscosity terms are added to stabilize the central differencing scheme.

The turbulence model used in the present study is based on the approach of Georgiadis et al [8] in which two algebraic models, one optimized for wall-bounded flows, and the other developed for unbounded flows are linked into a single model. For wall-bounded flow regions, the Baldwin-Lomax [9] turbulence model is used. In the unbounded regions, such as free shear layers, the Thomas [10] model is used. To provide a smooth transition from the bounded and unbounded regions, a link methodology similar to that proposed in Ref. [8] was employed. When using standard algebraic turbulent models, unrealistically high turbulent viscosities are often obtained, particularly in flows involving several streams and wall boundaries. As a result, it is usually necessary to artificially limit the maximum value that the turbulent eddy viscosity can have. By using the present approach, the artificial limiting of the eddy viscosity was not required. This is an important issue for the scaling studies described later in the paper. Constant turbulent Schmidt and Prandtl numbers were assumed ($Pr_t = Sc_t = 0.9$).

The code used for the external burning simulations has a generalized chemistry capability. However, since in the present study the injection process is not modeled in detail, the use of a detailed combustion model would be superfluous. Instead, we preferred to use a simple combustion model and leave the rate at which heat is released into the flow as a parameter that could be easily adjusted. This approach is consistent with our objective of investigating the effects of external heat release on the performance of SERN nozzles, and the effects of scale. The combustion model assumes a single reaction

$$2H_2 + O_2 + 3.76N_2 \rightarrow 2H_2O + 3.76N_2 \qquad (19)$$
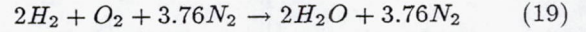
Therefore, only four species are considered, H_2, O_2, H_2O, and N_2. In the experiments, the only source of ignition for the external burning stream was contact with the adjacent hot nozzle exhaust plume. Therefore, in the present study, it is assumed that combustion starts at the trailing edge of the cowl. The rate of heat release is controlled by adjusting the reaction rate constant, K_f, and by assuming a flame spread angle. Experimental infrared images indicated that the flame spread angle remains in the relatively narrow range of 5° to 15°. In the present study, a flame spread angle of 10° was assumed for all the computations. The reaction rate constant was subsequently adjusted to produce pressure distributions similar to that obtained in the experiments. A single value for the reaction rate constant, $K_f = 6000$, was used for all the computations.

Force Data Reduction Scheme

The total force on the nozzle was considered to be the sum of three parts: an internal stream thrust, a ramp pressure force, and a cowl boat-tail force. The axial and normal components of the internal thrust are calculated from

$$F_{x,int} = \int_{exit} [\rho u^2 + (p - p_\infty)]dA_x \qquad (20)$$

$$F_{y,int} = \int_{exit} [\rho uv]dA_x \qquad (21)$$

The forces on the expansion ramp and boat-tail are computed by surface integration

$$F_{x,S} = \int_S [p - p_\infty]dA_x \qquad (22)$$

$$F_{y,S} = \int_S [p - p_\infty]dA_y \qquad (23)$$

where S denotes either the expansion ramp surface, or the boat-tail surfaces. The forces are normalized by the ideal (optimum) thrust coefficient, F_i, which is a function of the nozzle pressure ratio, NPR, and the specific heat ratio, γ, of the nozzle exhaust flow [11]

$$\frac{F_i}{p_\infty A_{th}} = \gamma NPR \sqrt{\frac{2}{\gamma - 1}(\frac{2}{\gamma + 1})^{\frac{\gamma+1}{\gamma-1}}} \sqrt{1 - (\frac{1}{NPR})^{\frac{\gamma-1}{\gamma}}} \qquad (24)$$

where A_{th} denotes the throat area.

In addition to the net total forces acting on the nozzle, a measure of the efficiency of the external burning process is needed. Here we use the specific impulse, I_{sp}, as the figure of merit. I_{sp} is generally defined as the net thrust per unit fuel flow, but for the present case, the magnitude of the force increment vector due to external burning is used. This force is directed at an angle given by its axial and normal components.

SERN Nozzle Configurations

The experimental investigation of nozzle performance and external burning was carried out using the NASA Lewis Jet Exit Rig [2]. This test rig, shown schematically in Fig. 7, was installed in the NASA Lewis 8' x 6' supersonic wind tunnel. The jet exit rig contains flow lines internal to the tunnel support strut that allowed a total air mass flow rate of 28 pounds-per-second split equally between two flow tubes. The hydrogen flow capacity was 0.4 pounds-per-second through a third flow tube. The hydrogen line is split at the flow measurement section to provide fuel to both the main combustor and an external burning fuel plenum. Up to 25% of the total hydrogen flow could be directed into the external burning plenum. After passing a flow metering station, the hydrogen and air were mixed and burned in the water cooled main combustor. The combustor was operated at a slightly lean fuel-air ratio to yield a temperature of about $3500°R$. The combustion products were then expanded through the SERN nozzle.

Two cowl configurations were used with a basic SERN nozzle model. A straight cowl was used as a "baseline" to determine the effects of cowl deflection and external burning. The SERN nozzle configuration with the baseline cowl is shown in Figs. 8(a) and (b). It had a 1-inch high throat followed by an expansion to an internal area ratio of 1.29 at the station where the expansion ramp begins, $x_r = 13.75$ inches. The expansion ramp was eight inches in width, had an initial angle of $17°$, and a trailing edge angle of $8°$. The length of the expansion ramp was $L = 27.47$ inches. Coordinates of the internal flowpath and the external expansion ramp are given in Ref. [2].

A deflected cowl configuration was designed to reduce overexpansion by reducing the internal area ratio, and also by generating an oblique shock that would impinge on the ramp's initial $17°$ corner. The throat area and location remained the same as the baseline cowl. The deflected cowl configuration is shown in Fig. 8(c). The $8°$ deflected portion terminated at the $x = 15$ inch station, extending 1.25 inches beyond the start of the expansion ramp.

In order to enhance flame stability, a flameholder could also be attached to the underside of the cowl, as shown in Fig. 9. The flameholder, positioned 2.5 inches downstream of the fuel injector, was a wedge with length of 1-inch and height of 0.5-inch.

Results

Code Validation; SERN Nozzles Without External Burning

A three-dimensional computation of a SERN nozzle at transonic flight conditions without external burning is presented first. The baseline nozzle was considered for a flight Mach number of $M = 1.2$, and a nozzle pressure ratio of $NPR = 4.97$. The stagnation temperature for the hot exhaust gas flow is $T_t = 1783°K$. The composition of the hot nozzle flow was determined from the fuel-air ratio used in the combustor, which in the present case was $F/A = 0.021$.

A five block grid consisting of a total of 220,000 points was used to model the nozzle and surrounding external flow. The domain extended to the trailing edge of the expansion ramp in the streamwise direction. Only half of the nozzle is computed since it was split at the plane of symmetry.

Figure 10 shows a particle trace plot that demonstrates the strong three-dimensional effect created in an overexpanded SERN nozzle. The low pressure in the nozzle plume gives rise to a transverse flow. Streamlines originating from the side of the nozzle are deflected towards the symmetry plane. The transverse flow tends to increase the magnitude of the pressure on the expansion ramp surface relative to a two-dimensional case. This is shown in Fig. 11 which plots the pressure coefficient on the expansion ramp surface as a function of the nondimensional distance measured from the start of the expansion ramp, x_r. Results for both the centerline and off-centerline (61% semi-width) are compared with both the experimental data of Ref. [2] and a two-dimensional calculation. The code appears to predict the three dimensional flow reasonably well, however, not enough grid points were used in the transverse direction in order to accurately resolve the flow around the side edges. This calculation required about 8 hours of CPU time on a CRAY YMP. Similar CFD studies of SERN nozzles without external burning have been performed previously by Yaros [12] and Koschel & Rick [13].

Attempting to extend this approach to model external burning would be prohibitively expensive for the following reason: when external burning is used, a large subsonic flow region is created which requires a flow domain that extends beyond the trailing edge of the expansion ramp. This fact combined with the need to improve the resolution in the transverse direction and resolve the injector and flameholding regions would significantly increase the number of points needed. Adding a detailed finite rate combustion model to the analysis could easily increase by an order of magnitude the computational resources needed. For this reason, the external burning flowfields are computed using the simplified model previously described.

Code Validation; SERN Nozzles With External Burning

Computations of several external burning nozzle configurations studied experimentally in Ref. [2] are presented

5

first. The computational domain that is used for the external burning study is schematically shown in Fig. 4. At the inflow boundary of the SERN nozzle the total pressure, total temperature and flow angle are specified, and a zero pressure gradient is assumed. The composition of the gases entering the nozzle is obtained from the fuel-air ratio used in the combustor upstream of the nozzle. At the inflow boundary of the external flow the pressure, temperature, and flow velocity are specified. The composition of the fueled stream-tube was determined from the global equivalence ratio obtained from the control volume analysis. All wall surfaces are treated as non-catalytic, no-slip boundaries, and a constant wall temperature $T_w = 300°K$ was assumed based on experimental data. The bottom surface is treated as a free boundary. The downstream boundary needs to be treated more carefully due to the subsonic region created by the external burning process. The subsonic region is embedded between two supersonic streams; one consisting of the exhaust plume, and the other consisting of the freestream flow. Far downstream of the expansion ramp trailing edge, the pressure field tends to become uniform, with the pressure field in the supersonic streams imposed on the subsonic stream. In the present study, the outflow boundary condition was applied at a distance $\frac{1}{2}L$ downstream of the expansion ramp trailing edge.

Four cases were considered for the code validation. The flow conditions and geometry used are given in Table 1. In addition, the following parameters were used in all four cases: nozzle total temperature, $T_{n,t} = 3500°R$, and external burning fuel total temperature, $T_{H_2} = 518°R$.

The first case investigated is the baseline nozzle without flameholder. Several grids having different spacings and number of points were examined. The computational domain was divided into 3 blocks, as shown in Fig. 12. The first and second blocks cover the internal nozzle and external flow up to the cowl tip respectively, and the third block covers the entire domain from the cowl tip downstream. For the baseline nozzle, 70 grid points in the horizontal direction were sufficient to accurately resolve the flowfield in the internal nozzle (block-1), and this number was not changed. Similarly, the flowfield around the cowl (block-2) was adequately modeled with 41 points in the horizontal direction. The number of points used in the vertical direction and the total number of points used for the third block was varied. Exponentially stretched increments in the vertical direction were used for all the grids. The values of y^+ for points nearest to the wall, for the fine grid, were below 5.

Figure 13 shows the pressure coefficient on the expansion ramp surface as a function of the nondimensional distance (measured from the start of the expansion ramp x_r) for three different grids. The results are compared with experimental data given at the centerline and off-centerline (61% semi-width) location. The station $(x - x_r)/L = 0$ corresponds to the the start of the expansion ramp, and the station $(x - x_r)/L = 1$ corresponds to its trailing edge. A coarse and a fine grid were investigated in addition to a fine, solution-adapted grid. All three grids give reasonably accurate results, but the finer grids give a better resolution of the double peak. The use of an adapted grid resulted in only a small improvement in the solution and does not justify the associated computational overhead. In all subsequent calculations, a distribution of points based on the fine grid was used.

In order to understand the effects of external burning on the pressure distribution along the expansion ramp, it is useful to view contour plots of various properties and compare them to the flow without external burning. Figure 14 shows contour plots for temperature, Mach number and pressure for the baseline nozzle with and without external burning[1]. Figure 14(a) presents temperature contour plots showing the high temperature external burning plume. The combustion process in the external stream creates a subsonic flow region embedded in two supersonic streams: one consisting of the exhaust plume and the other consisting of the freestream flow, as shown in fig. 14(b). The subsonic flow region is attained solely by the large increase in the sonic velocity due to combustion. The subsonic flow region created by the external burning process has important implications. In addition to local high pressure regions created by external burning, information can now propagate upstream through this subsonic zone, and higher back pressure levels can be imposed also along the entire expansion ramp surface. The local high pressure created by the external burning plume can be strong enough to cause boundary layer separation. This appears to be the case for the present flow conditions, as seen in the Mach number contour plot and the pressure coefficient plot (fig. 13). A small separation bubble appears around the station $(x - x_r)/L = 0.2$. The pressure increase behaves like a classic separated boundary layer, with a pressure rise due to the separation shock followed by a pressure plateau and a second jump due to the reattachment shock. The subsequent pressure variations are a result of reflected waves from the shear layer and further interactions with the external burning plume. Figure 14(c) shows the effect of external burning on the pressure field. Note the localized high pressure areas and the pressurization of almost the entire flowfield to atmospheric levels. Also, note that the pressure at the exit boundary is nearly uniform, consistent with our treatment of the outflow boundary condition.

The second case investigated considered the deflected cowl without flameholder. The internal block required 105 grid points in the horizontal direction. The extra grid

---

[1]The results shown in Fig. 14 without external burning give only qualitative information, since they do not include 3D effects

points were needed to resolve the internal shock. The rest of the grid used a distribution of points similar to that used for the baseline cowl. Figure 15 shows the pressure coefficient on the expansion ramp surface. The computed results appear to predict the general trend observed in the experiments, however, the computed peak values appear to be slightly damped. The pressure spike near station $(x - x_r)/L = 0$ is caused by the oblique shock generated by the deflected cowl impinging slightly ahead of the 17° expansion ramp corner.

The next two cases considered the deflected cowl with the flameholder shown in Fig. 9. A fourth block was added to the grid topology. Figure 16 shows the pressure coefficient for the $M = 1.8$ case. Once again, the computed pressure distribution is in close agreement with the experiments, however, the pressure peak appears to be overpredicted. Figure 17 presents results for the same configuration at $M = 1.2$. The agreement with the experiments is not as good as in the previous cases, but the general trend is well predicted by the computations. It should be pointed out that the first pressure peak, which is underpredicted, is experimentally observed along the centerline but not at the off-center location. A typical computation required approximately 90 minutes of CPU time on the CRAY YMP.

Figure 18 shows a qualitative comparison for this case between experimental infrared images and computational results (temperature contours). The bright spots around the nozzle exit are due to hot metal radiation, as well as the bright area near the uncooled end of the expansion ramp surface. Surface reflections may be responsible for some of the bright spots not observed in the CFD result.

The individual terms comprising the axial and normal forces for the four cases discussed above are shown in Fig. 19. The internal, ramp, and boat-tail parts of the total force are displayed in bar charts and compared with the experimental results of Ref. [2] with and without external burning. Three observations must be made regarding this figure. First, the boat-tail pressures were not measured in Ref. [2], but they were estimated using the projected areas and a base pressure assumption. The values obtained in the present work provide a better approximation to these forces and they have been used to complement the other forces obtained from Ref. [2]. Second, since experimental pressure measurements extended only up to station $(x - x_r)/L = 0.61$, the CFD ramp surface pressure was integrated up to this point also. Third, following Ref. [2], the flameholder forces have been neglected. This is due to the fact that, in the experiment, a disproportionately large flameholder was required at the model scale to stabilize the flame. If these forces were included, the results would not be representative of the full scale nozzle.

From this figure it is clear that external burning in-

creases the ramp and cowl boat-tail forces in both the axial and normal directions. The effect of external burning is more pronounced in the normal forces. Negative nozzle normal force is detrimental to vehicle performance because additional lift, and therefore induced drag, is required to counteract it. Also, the resultant nose-up moment must be compensated for, usually by control surface deflection with an associated drag penalty.

The increase in total axial and normal forces as a percentage of ideal axial force, predicted by the present study and by the experimental work of Trefny and Carboni is shown in Table 2. With the exception of case-3, for which the CFD results overpredict the force increments relative to the experiment, the computations differ from the experimental values by 10-20%.

The force increments range from 4% to 14% in the axial direction, and from 16% to 58% in the normal direction.

The effectiveness of external burning is also demonstrated in Table 2, which shows the specific impulse obtained from the present study, and from the results of Ref. [2]. The computed I_{sp} values range from 554 to 2722 seconds, compared with a range from 609 to 2113 seconds reported by Trefny and Carboni. The lower I_{sp} values are obtained with the baseline cowl. For comparison, the I_{sp} of other auxiliary propulsion methods, such as a chemical rocket, have an I_{sp} of about 400. One disadvantage of external burning is that there is little control, if any, of the direction of the total force vector increment.

Effect of External Burning Fuel Pressure on SERN Nozzles

The variation of external burning performance with fuel pressure is shown in Figs. 20-22. The deflected cowl with flameholder at $M = 1.2$ and a nominal $NPR = 6$ is considered. The pressure distribution on the expansion ramp is shown in Fig. 20 for four different fuel injection pressures. The corresponding global equivalence ratio is also indicated in this figure. The net effect of increasing the fuel pressure is the reduction of the amount of overexpansion on the initial part of the ramp and the creation of a second pressure peak which starts near the trailing edge of the expansion ramp and moves upstream with still higher values of the fuel pressure. This same trend has been observed in the experiments of Ref. [2]. The effect on the resulting forces is shown in Fig. 21. The axial and normal forces on the expansion ramp and cowl boat-tail progressively increase with fuel pressure over this range. The pressures on the expansion ramp were integrated up to the trailing edge in this case. It should be pointed out that at the lowest fuel pressure, the forces are probably underestimated. The reduced amount of external heat addition cannot raise the pressure to atmospheric levels, and therefore, three dimensional effects could be expected to increase the normal and axial forces calculated for this

case. The total axial and normal forces as a function of external burning fuel pressure are shown in Fig. 22 and are compared with experimental data. Note that the axial and normal forces show an increasing trend in both CFD and experiment over this fuel injection pressure range, although at a different rate. One possible source for this difference could be the fact that the experimental result is based on ramp pressure data up to $(x - x_r)/L = 0.61$. The CFD results, however, considered the entire expansion ramp. Eventually, the force curves of Fig. 22 will level out at still higher fuel pressures. The value at which this will occur has not been determined.

Figure 23 shows Mach number contour plots for the four fuel pressures. The constraining effect of the external burning process on the nozzle plume expansion is clearly visible in this figure. Note that an increased fuel pressure results in a reduction in the initial expansion. The external burning plume deflects the shear layer towards the expansion ramp, creating a converging area for the internal nozzle plume. The decrease in area for this supersonic stream results in a decrease in Mach number which produces the first pressure peak.

Performance of External Burning as a Function of NPR

The performance of a SERN nozzle over a range of nozzle pressure ratios is investigated at two Mach numbers $M = 1.2$ and $M = 1.8$. The deflected cowl with a flameholder is analyzed for a fixed fuel injector pressure of $p_{H_2} = 320.4$ for the $M = 1.2$ case, and $p_{H_2} = 112.9$ for the $M = 1.8$ case. Figure 24 shows the variation in the pressure coefficient on the expansion ramp with NPR for the two Mach numbers. The flat pressure distribution at the lowest NPR indicates that the external burning plume is effectively preventing any further overexpansion beyond the cowl trailing edge. This flat, nearly uniform ambient pressure distribution is in agreement with experimental observations [2]. As NPR is increased, the pressure on the initial portion of the ramp increases accordingly, but subsequently drops sharply. The effect of external burning on the pressure distribution is felt further downstream as the NPR increases.

Figure 25 shows temperature contours for the four NPR values at $M = 1.8$. The internal nozzle plume grows in size with increasing NPR, and is able to penetrate further downstream against the constraining force of the external burning plume. Note that for the lowest NPR, a high temperature region is established around the cowl boat-tail. At the higher NPRs the high temperature created by the external burning process cannot propagate upstream to the cowl. This may help explain the difficulties encountered by Trefny and Carboni [2] in stabilizing an external burning flame a high NPR values ($NPR > 8$).

The nozzle force components for the $M = 1.8$ case is shown in Fig. 26. The internal axial force ratio decreases with NPR because the internal expansion area remains constant. The decrease in internal thrust is compensated for by an increase in the ramp forces due to the larger pressures acting on its surface. The magnitude of the boat-tail forces increases initially because at $NPR = 8.5$ the external combustion region does not extend back to the cowl region. At higher NPR values, boat-tail forces decrease in magnitude as they become progressively smaller compared to the ideal axial force. The total axial and normal forces as a function of NPR are plotted in Fig. 27. They are compared with the experimental results of Trefny and Carboni [2] with and without external burning. In the experimental study, an external burning flame could not be stabilized at NPR values greater than 8, as previously mentioned, therefore only one data point is plotted. The practical stabilization of an external burning flame at high NPR values will require further study.

Scaling Studies

The computations presented above considered a 10% scale model. There is considerable interest in exploring the performance of external burning in a full scale nozzle. Two full scale (100%) configurations were studied. In the first one, the whole nozzle including the flameholder was scaled up by a factor of 10. The second configuration takes into account the fact that if a 0.5-inch flameholder stabilizes combustion at model scale, then the same 0.5-inch step should stabilize a piloting flame at vehicle scale if pressure, temperature, velocity and fuel pressure are comparable. From a practical standpoint, however, some increase in flameholder height would be required since the boundary layer and the fueled stream height would scale geometrically. The scale factor required for the flameholder is presently unknown but thought to be much less than the model scale factor. Therefore, the second 100% scale configuration considers a scale up of the entire nozzle except for the flameholder which is kept at 0.5-inch height.

In order to maintain the same resolution of the boundary layer at full scale, where the Reynolds number is 10 times larger, the clustering of grid points near the wall was increased by a factor of $\sqrt{10}$. This factor will keep the value of y^+ unchanged, since it is proportional to the distance from the wall, and to the square root of the Reynolds number.

The kinetics of the combustion process is independent of scale, and for the same flow velocity, the flame propagation angle should be identical also. Therefore, the parameters controlling the rate of heat release were not modified for the full scale computations.

8

Figure 28 shows the pressure coefficient for the 10% scale nozzle, the 100% scale nozzle, and the 100% scale nozzle with the 0.5-inch flameholder. The data is presented for $M = 1.2$, and $M = 1.8$. The results indicate that there is practically no effect of scale on the pressure distribution. The flowfield in the 10% scale nozzle and the overall 100% nozzle are nearly identical. Some differences are observed when the flameholder is kept at 10% scale (0.5-inch). This effect is due to the change in the shear layer flow, resulting from a difference in the relative scales between the nozzle and flameholder. The Mach number contours for the 10% nozzle and the 100% nozzle with the 10% scale flameholder at $M = 1.2$ is shown in Fig. 29. A detail of the flow near the flameholder is shown in part (c) of Fig. 29.

Conclusions

A computational investigation of the effects of external burning on the performance of SERN nozzles operating at transonic speeds was presented. The study focused on the effects of external heat addition and introduced a simplified injection and mixing model based on a control volume analysis. This simplified model permitted parametric and scaling studies that would have been prohibitively costly to conduct with a detailed CFD analysis.

While overexpanded SERN nozzles without external burning required a full three dimensional analysis, it was shown that SERN nozzles that include external burning can be adequately modeled using a two-dimensional formulation. The CFD methodology was validated by comparing the computed pressure distribution and thrust forces with experimental data. These comparisons were conducted for several nozzle configurations at various flow conditions. Good agreement between computational and experimental results was obtained. Specific Impulse calculations were also presented which indicated that external burning performance can be superior to other forms of thrust augmentation methods at transonic speeds. The results show that external burning can pressurize not only the expansion ramp, but also the nozzle cowl surface.

The effects of injection fuel pressure and nozzle pressure ratio on the performance of SERN nozzles with external burning were investigated. The external burning process was shown to create a large subsonic flow region that permits higher back pressure levels to be imposed along the expansion ramp. In addition, localized high pressure regions are created by the external burning process. The adverse pressure gradients established, can force the boundary layer to separate. This interaction may be a major design issue and will require further study. The results of the parametric studies produced trends similar to those reported in the experimental study, and provided additional information that complements the experimental data, improving our understanding of external burning flowfields. A study of external burning at full scale was also presented. The results indicated that the flowfield is not very sensitive to scale.

References

[1] Trefny, C. J., "Experiments and Analysis Concerning the Use of External Burning to Reduce Aerospace Vehicle Transonic Drag," NASA TM-105397, Jan. 1992.

[2] Trefny, C. J. and Carboni, J.D., "Results of a Single-Expansion-Ramp Nozzle Experiment With Hot Exhaust and External Burning," NASA TM-106390, 1993.

[3] Bittner, R.D. and McClinton, C.R., "Numerical Study of External Burning Flowfields," AIAA paper 91-2392, June 1991.

[4] Povinelli, F.P. and Povinelli, L.A., "Correlation of Secondary Sonic and Supersonic Gaseous Jet Penetration Into Supersonic Crossflows," NASA TN D-6370, June 1971.

[5] Yungster, S., "Numerical Study of Shock-Wave Boundary Layer Interactions in Premixed Combustible Gases," *AIAA Journal*, Vol. 30, No. 10, 1992, pp. 2379-2387.

[6] Yee, H.C., Klopfer, G.H. and Montagnè, J.-L., "High-Resolution Shock-Capturing Schemes for Inviscid and Viscous Hypersonic Flows," NASA TM-100097, Apr. 1988.

[7] Chitsomboon, T., private communication, ICOMP-NASA Lewis Research Center, Cleveland, OH, March 1993.

[8] Georgiadis, N.J., Drummond, J.E. and Leonard, B.P., "Development of an Algebraic Turbulence Model for Analysis of Propulsion Flows," AIAA paper 92-3861, 1992.

[9] Baldwin, B. and Lomax, H., "Thin Layer Approximation and Algebraic Model for Separated Turbulent Flows," AIAA paper 78-257, Jan. 1978.

[10] Thomas, P.D., "Numerical Method for Predicting Flow Characteristics and Performance of Nonaxisymmetric Nozzles, Theory," NASA CR-3147, Sept. 1979.

[11] Hill, P.G. and Peterson, C.R., *Mechanics and Thermodynamics of Propulsion,* 1st ed., Addison-Wesley, 1965, pp. 354-362.

[12] Yaros, S., "Use of the PARC Code For Generic NASP Nozzles Operating at Off-Design Transonic Conditions," AIAA paper 91-2154, June 1991.

[13] Koschel, W. and Rick, W., "Design Considerations for Nozzles of Hypersonic Airbreathing Propulsion," AIAA paper 91-5019, Dec. 1991.

Table 1: Code Validation Cases

Case	Cowl	Flameholder	Mach number	NPR	p_{H_2} psi	p_∞ psi	$(F/A)^a$
1	baseline	no	1.2	6.07	320.0	6.87	0.021
2	deflected	no	1.2	5.37	238.4	6.87	0.016
3	deflected	yes	1.8	8.58	112.9	4.0	0.018
4	deflected	yes	1.2	6.45	320.4	6.87	0.02

[a]Fuel-air ratio in the combustor (nozzle inlet)

Table 2: Performance of External Burning

Case	$(\Delta F/F_i)_x$		$(\Delta F/F_i)_y$		I_{sp} (sec)	
	Experiment	CFD	Experiment	CFD	Experiment	CFD
1	0.053	0.047	0.178	0.162	609	554
2	0.136	0.146	0.448	0.545	1768	2131
3	0.043	0.063	0.178	0.326	1501	2722
4	0.140	0.121	0.584	0.513	2113	1857
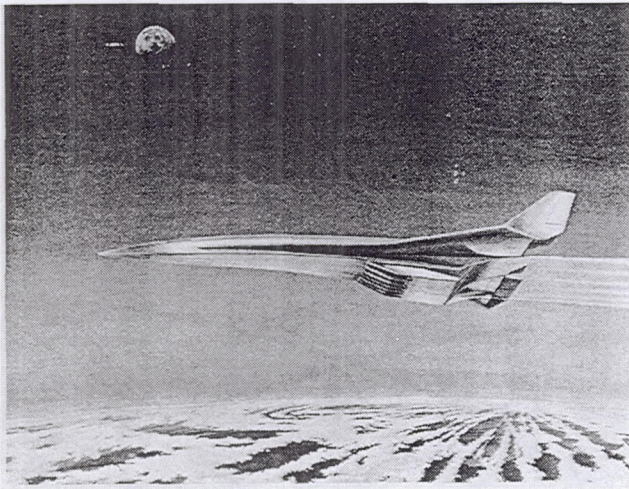
Fig. 1. Artists conception of a single-stage-to-orbit vehicle.
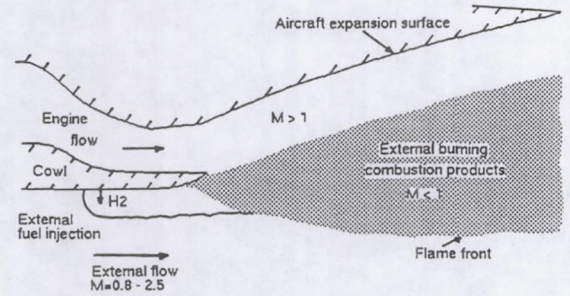
Fig. 3. Schematic of external burning.
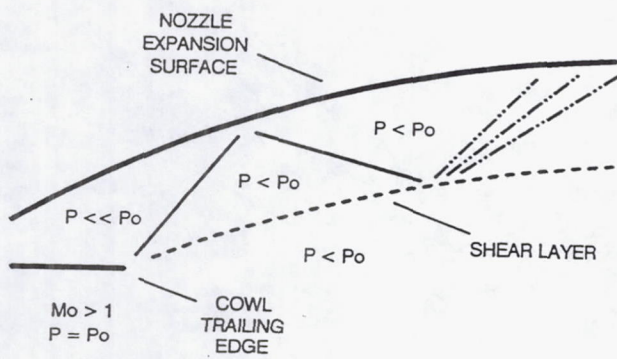
Fig. 2. Schematic of over-expanded SERN nozzle at transonic conditions.
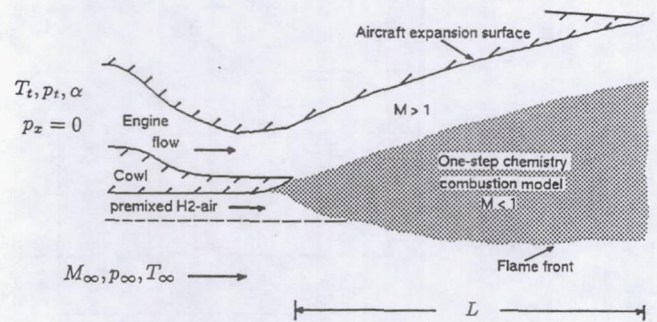
Fig. 4. Computational model of external burning.
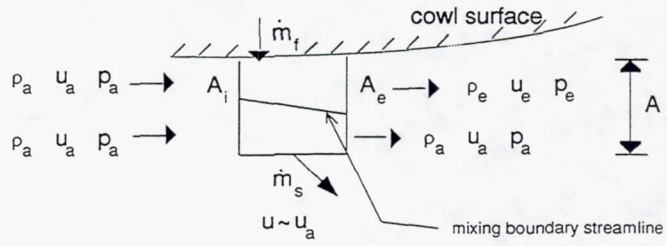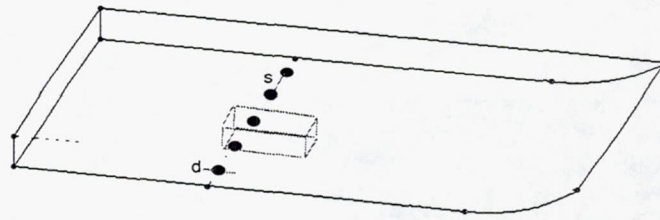
Fig. 5. Control volume analysis of the flow around the fuel injector.
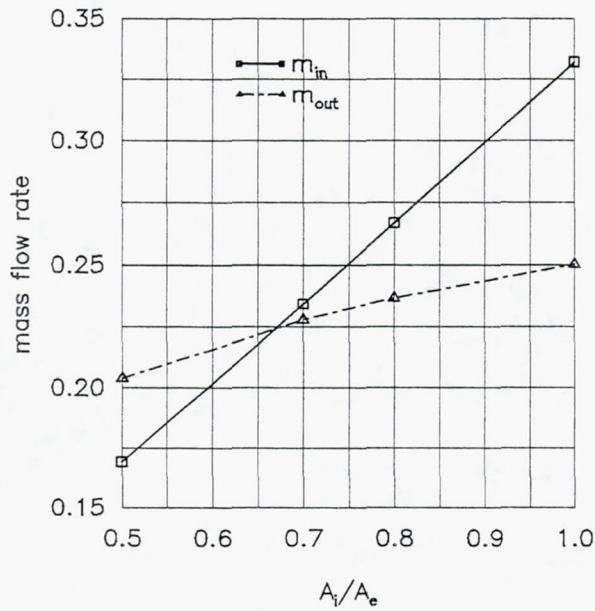
Fig. 6. Graphic solution of Eq. 15.
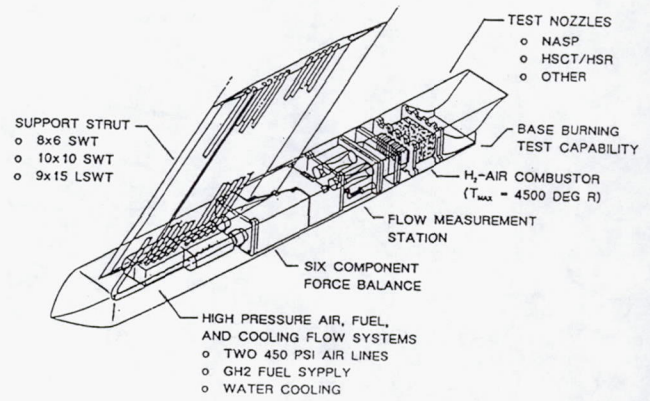
Fig. 7. Schematic of NASA Lewis jet exit rig.

(a) Nozzle geometry with baseline cowl.

8° trailing edge angle

Nozzle Ramp Surface (Upper Wall)
Coordinates in Table 1(a)

17° initial angle

Baseline Cowl

L

x

Combustor Exit
(Nozzle Inlet)

Throat
x_t=9.875 x_T=13.75

(b) Baseline Cowl

Cowl Internal (Lower Wall)

Straight line

8.875 Radius centered at x=10.125

0.888

0.066 Radius

x=10.125 x_T=13.75

(c) Deflected Cowl

Cowl Internal (Lower Wall)
Coordinates Same as Baseline
Up to x=12.70

8° deflection

Straight line

1.211

0.063 Radius

Straight line blend into 8.875 Radius

x=12.70

x=15.00

Fig. 8. Schematic of SERN nozzle configurations.

8 DEGREE
DEFLECTION

2.825

.50

1.00

FUEL INJECTION
.381" SPACING
21, .060" DIA.
(S/d = 6.35)

2.50 (42 dia)

5.50 (92 dia)
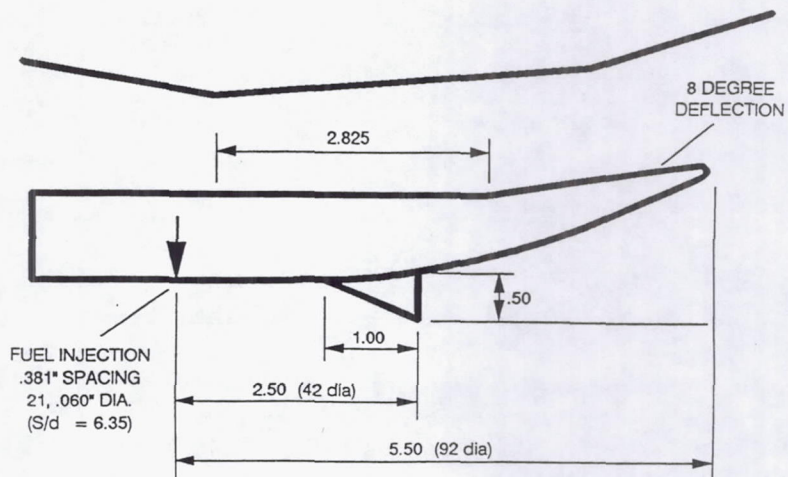
Fig. 9. Schematic of flameholder.

13
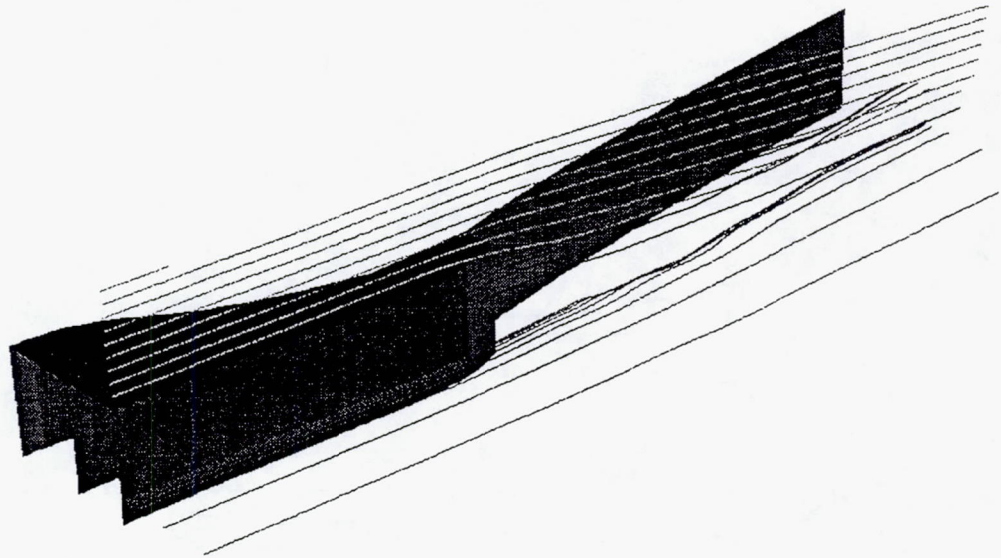
Fig. 10. Particle traces for a SERN nozzle without external burning. $M_\infty = 1.2$.
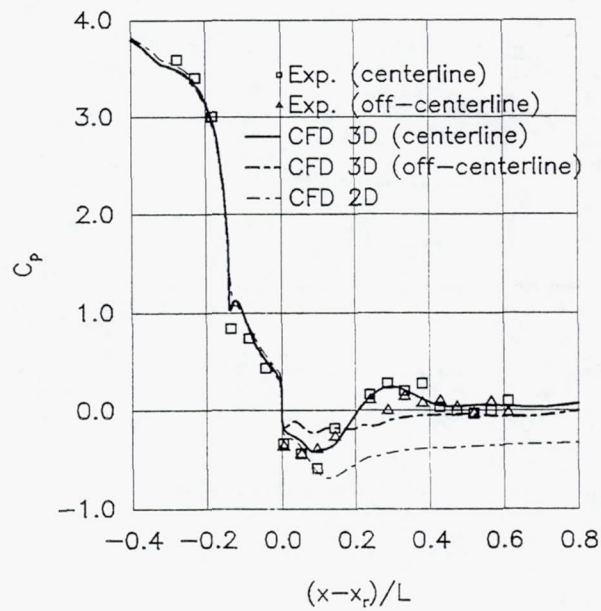
Fig. 11. Pressure coefficient on the expansion ramp surface without external burning.
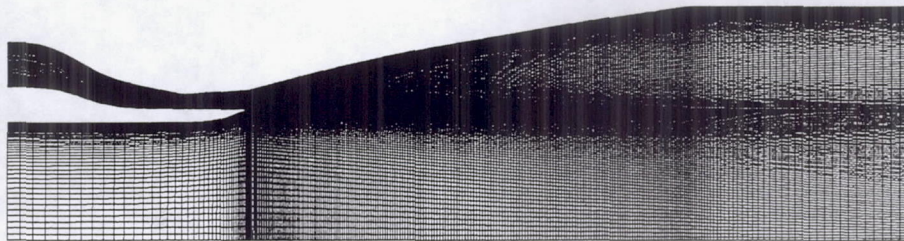
Fig. 12. Computational grid. 3 blocks 70x93; 40x65; 240x158.
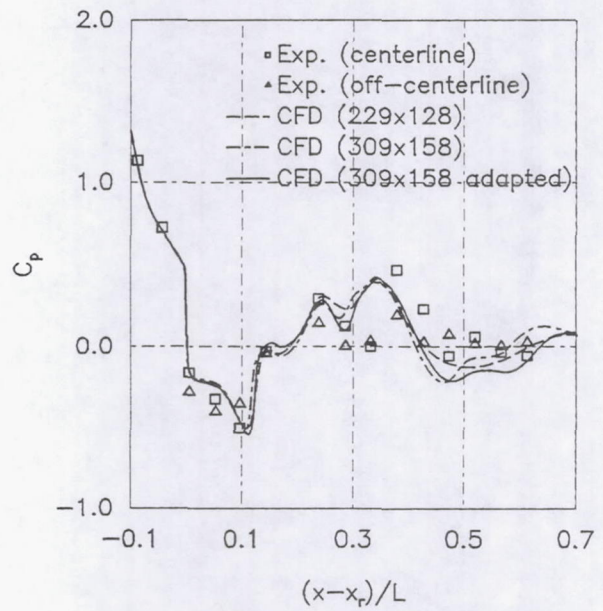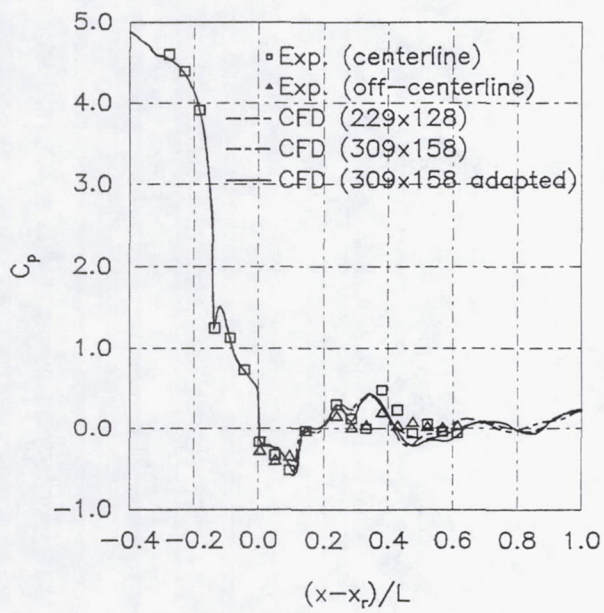
Fig. 13. Pressure coefficient for three grid distributions. Baseline nozzle, no flameholder, $M_\infty = 1.2$, $NPR = 6.07$.

(a)

(b)

No EB.

No EB.

| 0.50000 |
| 1.00000 |
| 1.50000 |
| 2.00000 |
| 2.50000 |
| 3.00000 |
| 3.50000 |
| 4.00000 |
| 4.50000 |
| 5.00000 |
| 5.50000 |
| 6.00000 |
| 6.50000 |
| 7.00000 |
| 7.50000 |

| 0.00000 |
| 0.20000 |
| 0.40000 |
| 0.60000 |
| 0.80000 |
| 1.00000 |
| 1.20000 |
| 1.40000 |
| 1.60000 |
| 1.80000 |
| 2.00000 |
| 2.20000 |
| 2.40000 |
| 2.60000 |
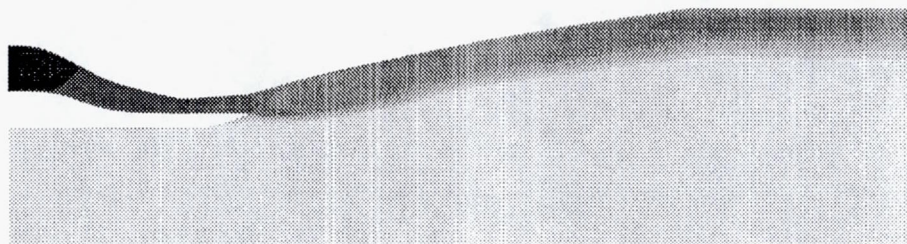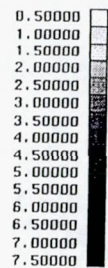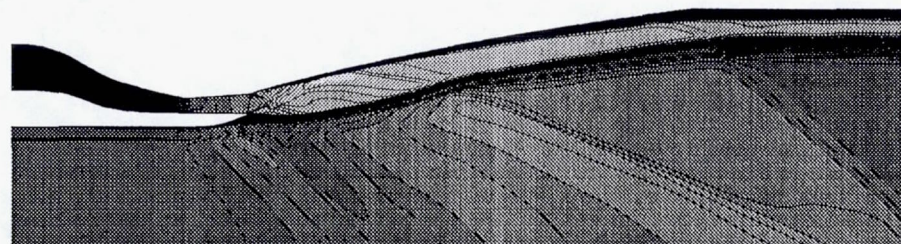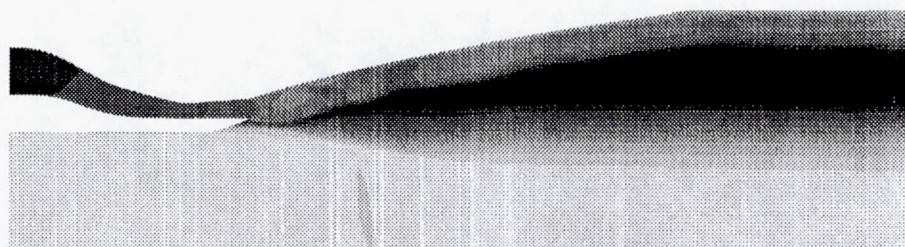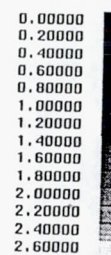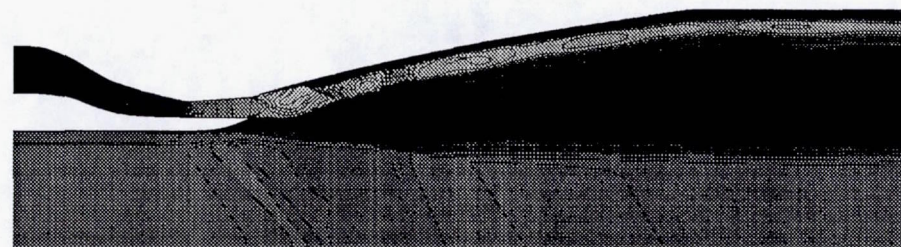
EB on

EB on

Fig. 14. Contour plot for baseline nozzle at $M_\infty = 1.2$. (a) Nondimensional temperature contours (T/T_∞); (b) Mach number contours.

(c)
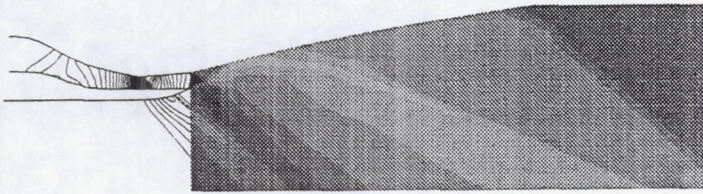
No EB.
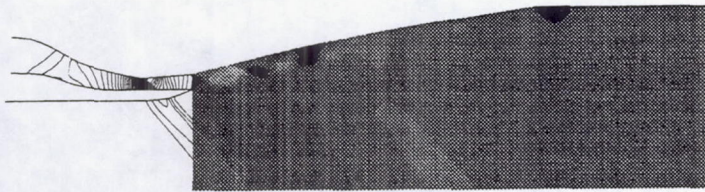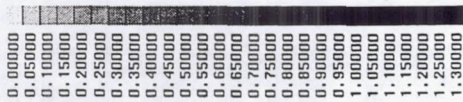
EB on

Fig. 14. cont. (c) Nondimensional pressure contours (p/p_∞).
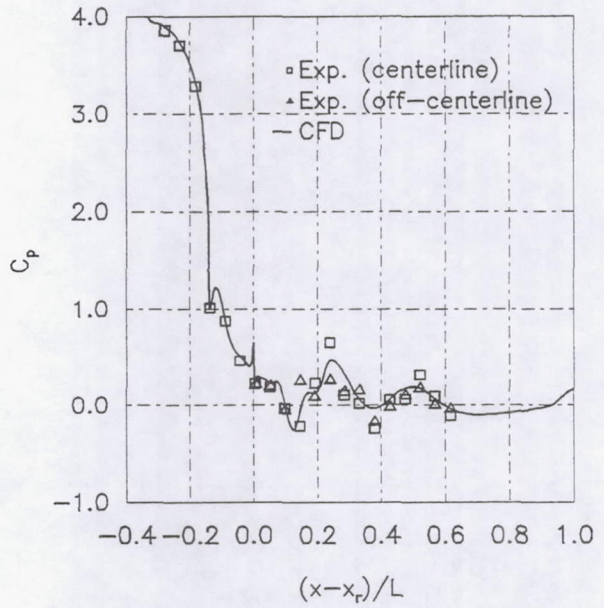
Fig. 15. Pressure coefficient for deflected cowl without flameholder. $M_\infty = 1.2$, $NPR = 5.37$.
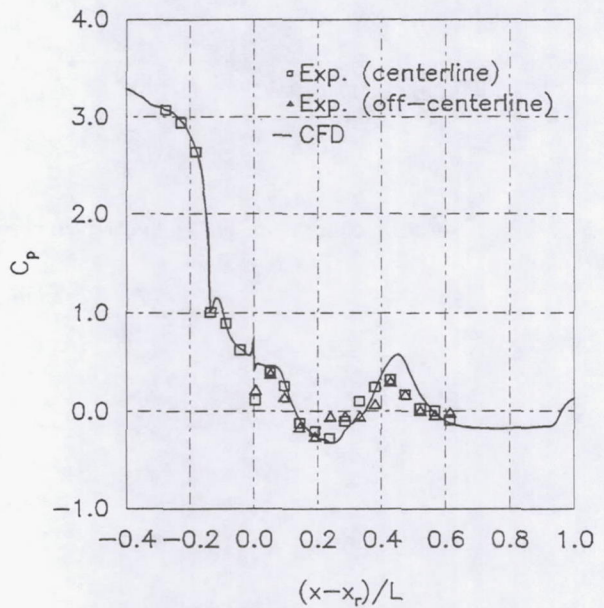
Fig. 16. Pressure coefficient for deflected cowl with flameholder. $M_\infty = 1.8$, $NPR = 8.58$.
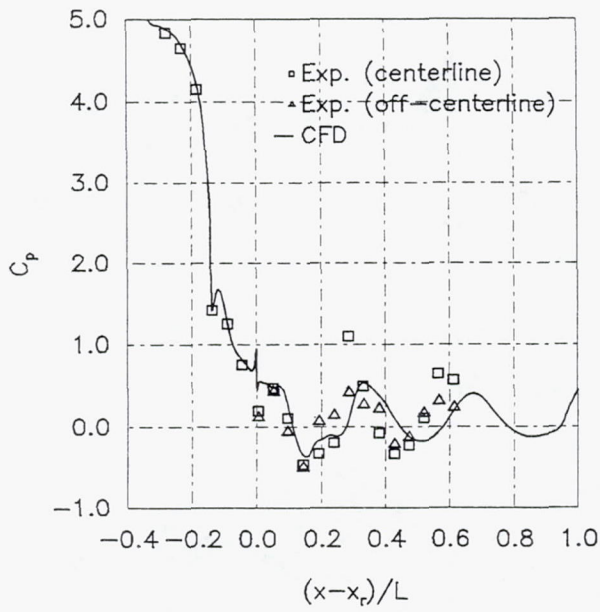
17

Experimental infrared image

Fig. 17. Pressure coefficient for deflected cowl with flameholder. $M_\infty = 1.2$, $NPR = 6.45$.
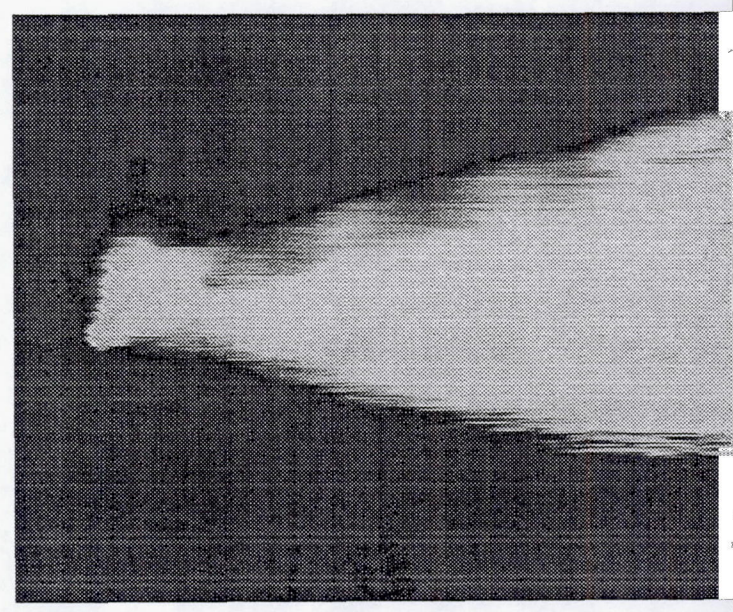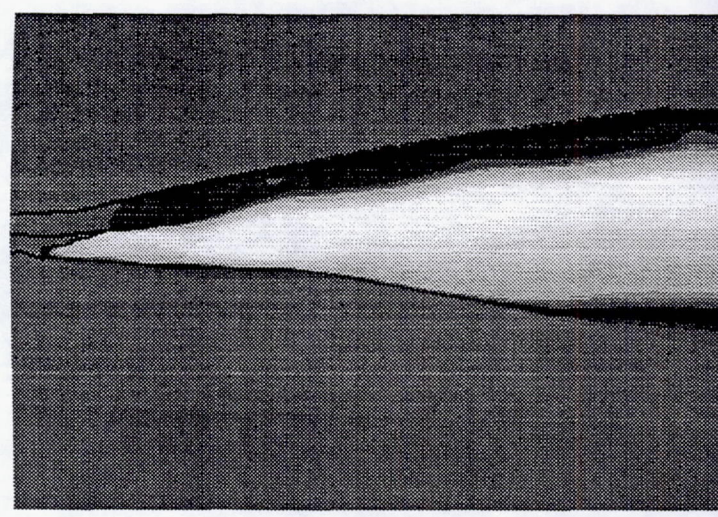
Computational result (T/T_∞).

Fig. 18. Qualitative comparison of computed and experimental external burning flowfield

(a)

(b)
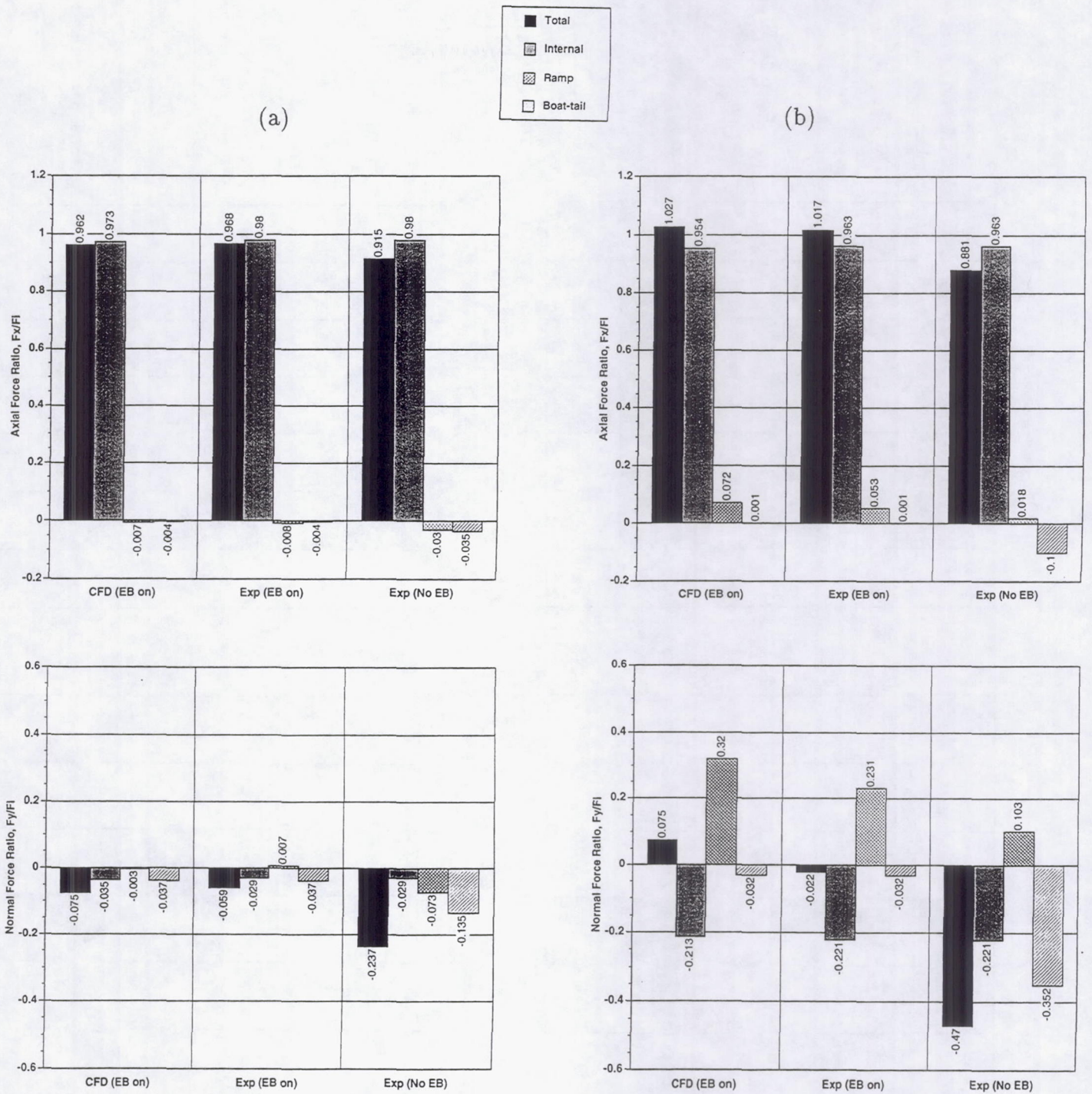
Fig. 19. Nozzle force components obtained with present CFD method, compared with the experimental results of Trefny and Carboni. (Note: The forces on the boat-tail were not measured in the experiments. Therefore, the values shown are those obtained in the present work.)
(a) Baseline cowl without flameholder, $M_\infty = 1.2$, $NPR = 6.08$. (b) Deflected cowl without flameholder, $M_\infty = 1.2$, $NPR = 5.37$.
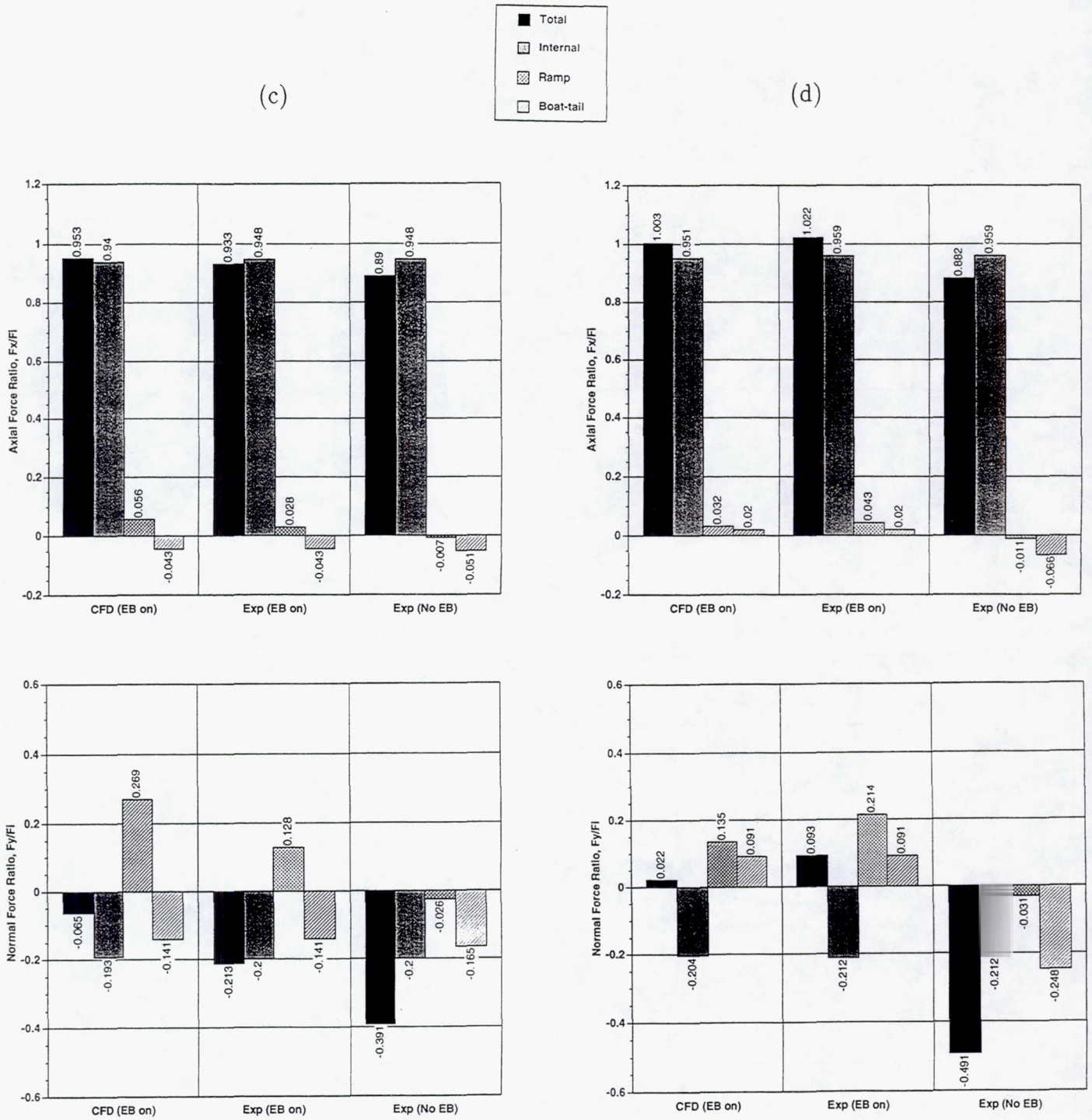
Fig. 19. continued. (c) Deflected cowl with flameholder, $M_\infty = 1.8$, $NPR = 8.58$. (d) Deflected cowl with flameholder, $M_\infty = 1.2$, $NPR = 6.45$.
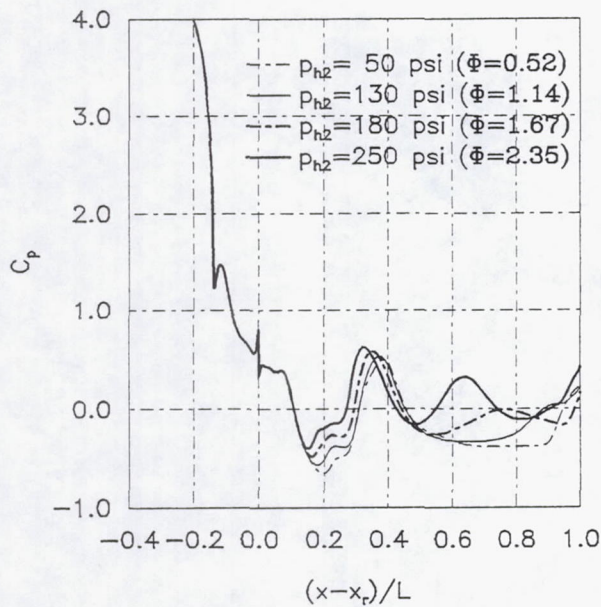
Fig. 20. Variation of pressure coefficient with external burning fuel pressure. $M_\infty = 1.2$, $NPR = 6$.
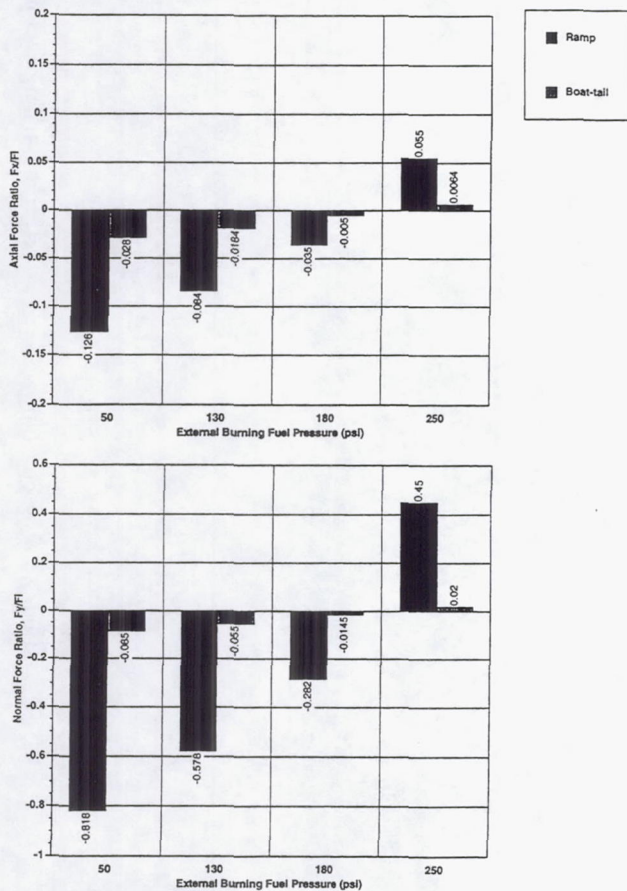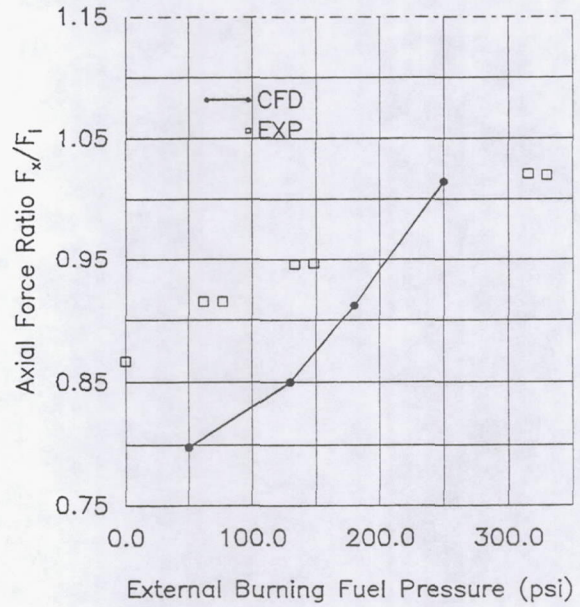
Fig. 21. Ramp and boat-tail forces variation with external burning fuel pressure.
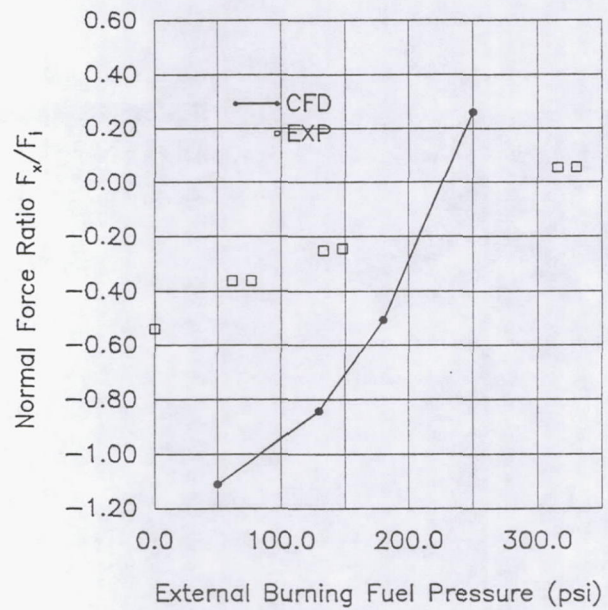
Fig. 22. Net (total) axial and normal forces as a function of external burning fuel pressure. $M_\infty = 1.2$, $NPR = 6$.

21
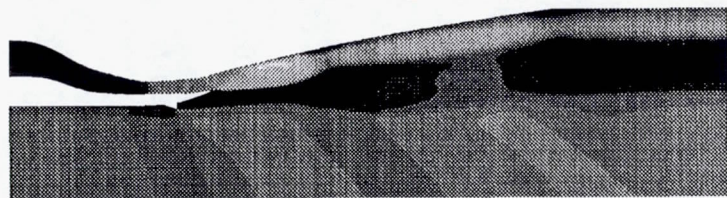
$p_{H_2} = 50$ psi $(\phi = 0.52)$
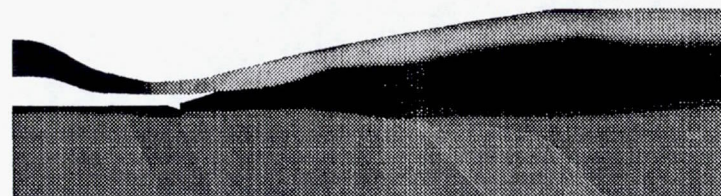
$p_{H_2} = 180$ psi $(\phi = 1.67)$
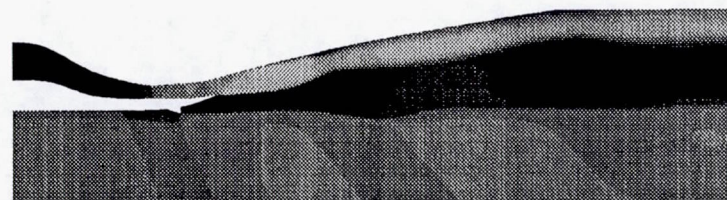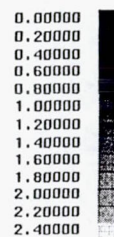
$p_{H_2} = 130$ psi $(\phi = 1.14)$
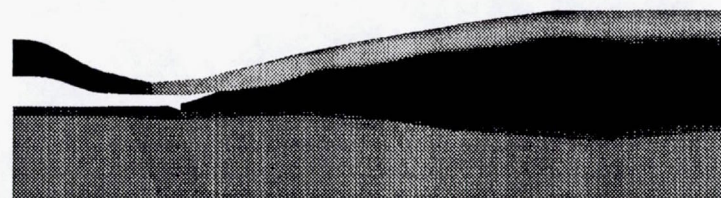
$p_{H_2} = 250$ psi $(\phi = 2.35)$

Fig. 23. Mach number contours at several external burning fuel pressures. $M_\infty = 1.2$, $NPR = 6$.
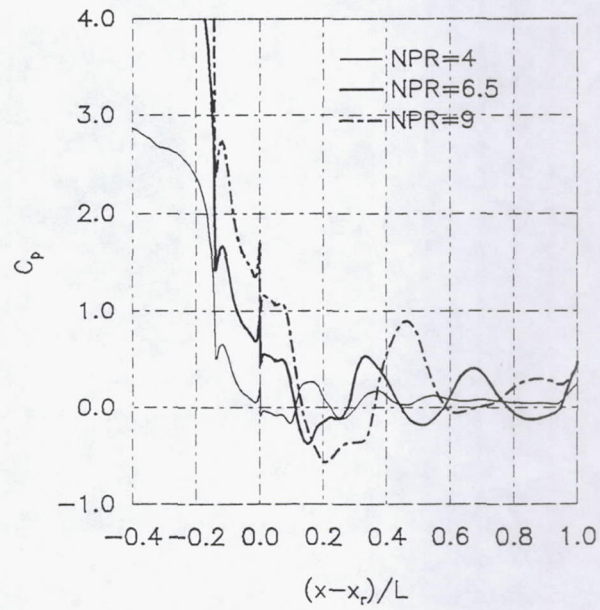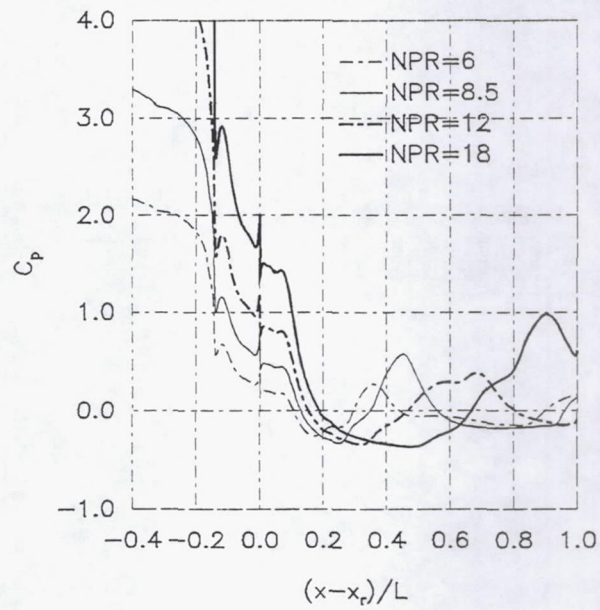
Fig. 24. Variation of pressure coefficient with nozzle pressure ratio at two Mach numbers: (a) $M_\infty = 1.2$, and (b) $M_\infty = 1.8$
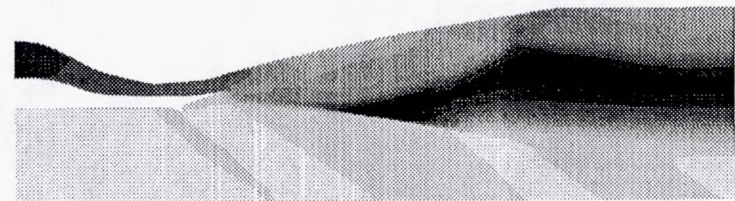
NPR = 6

NPR = 12

0.50000	
1.00000	
1.50000	
2.00000	
2.50000	
3.00000	
3.50000	
4.00000	
4.50000	
5.00000	
5.50000	
6.00000	
6.50000	
7.00000	
7.50000	
8.00000	
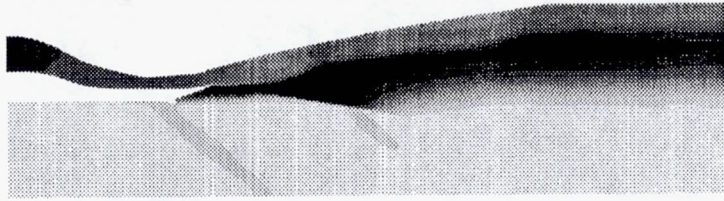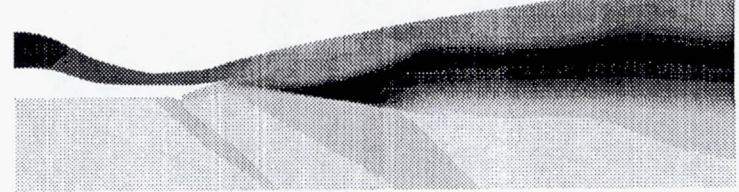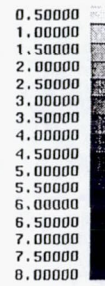
NPR = 8.5

NPR = 18

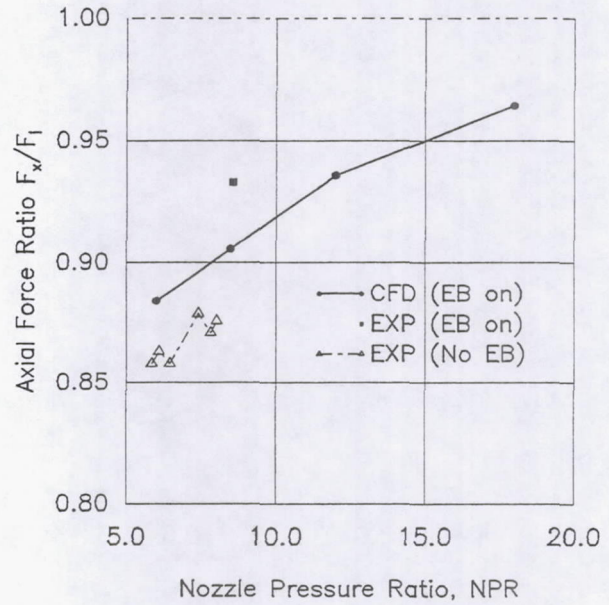Fig. 25. Temperature contours (T/T_∞) at several nozzle pressure ratios. $M_\infty = 1.8$, $p_{H_2} = 112.9$.
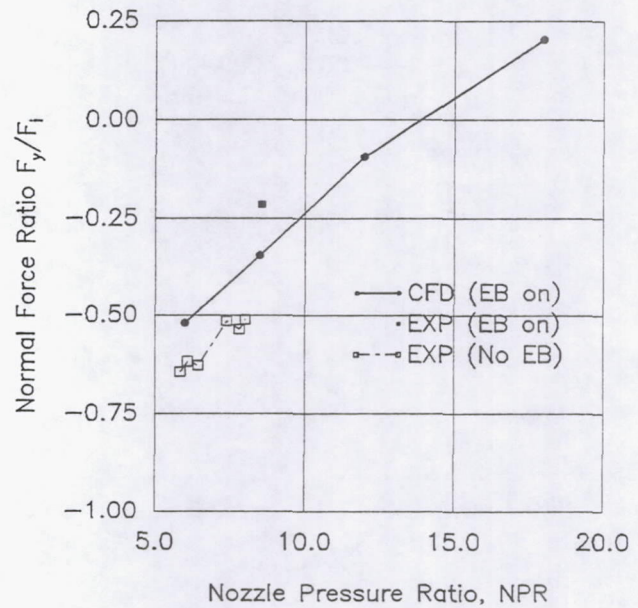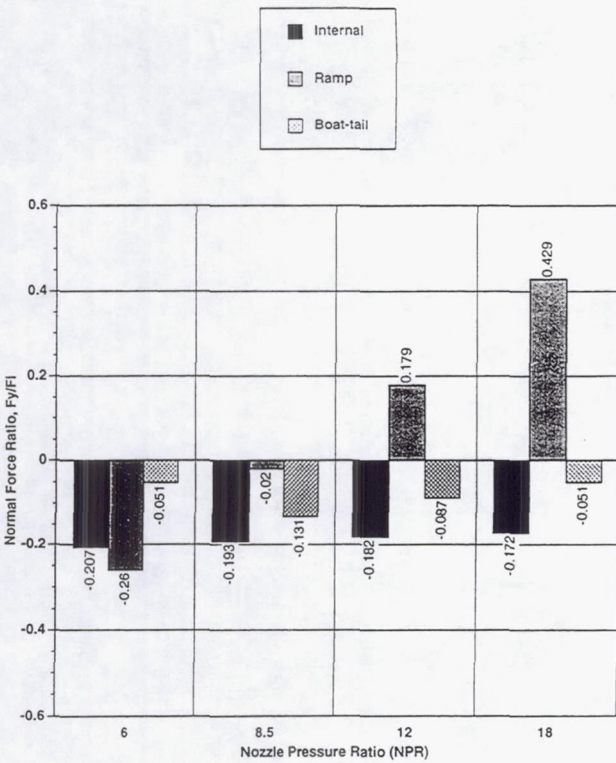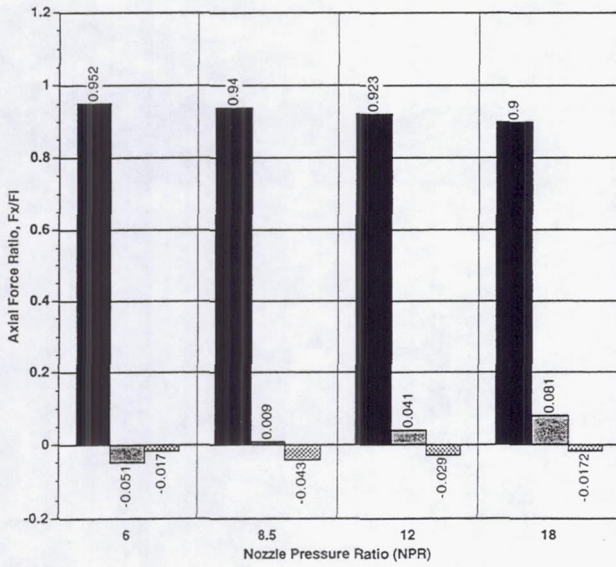
Fig. 26. Nozzle force component variation with nozzle pressure ratio (NPR). $M_\infty = 1.8$, $p_{H_2} = 112.9$.

Fig. 27. Net (total) axial and normal forces as a function of nozzle pressure ratio, compared with the experimental results of Trefny and Carboni with and without external burning. $M_\infty = 1.8$, $p_{H_2} = 112.9$.
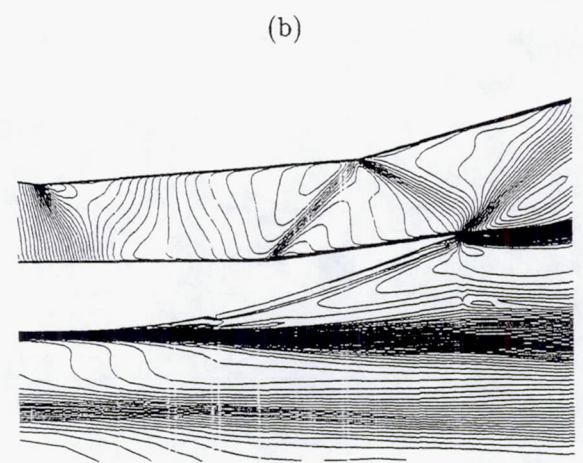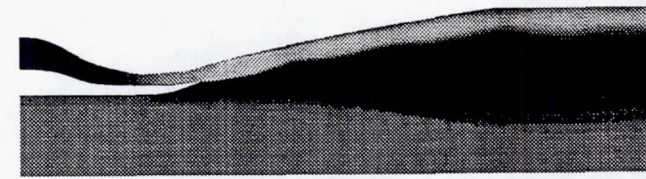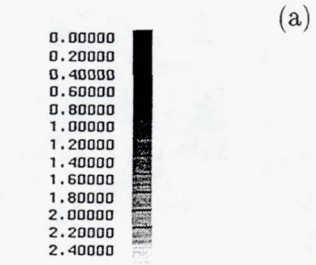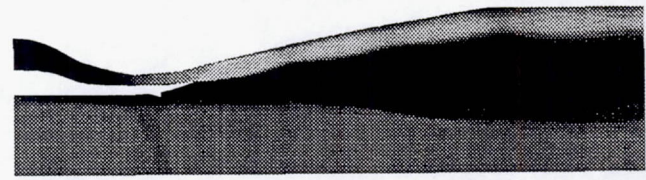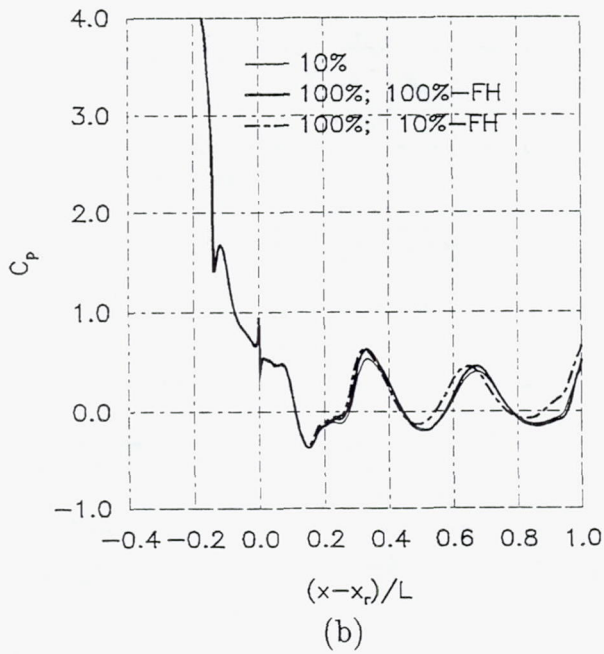
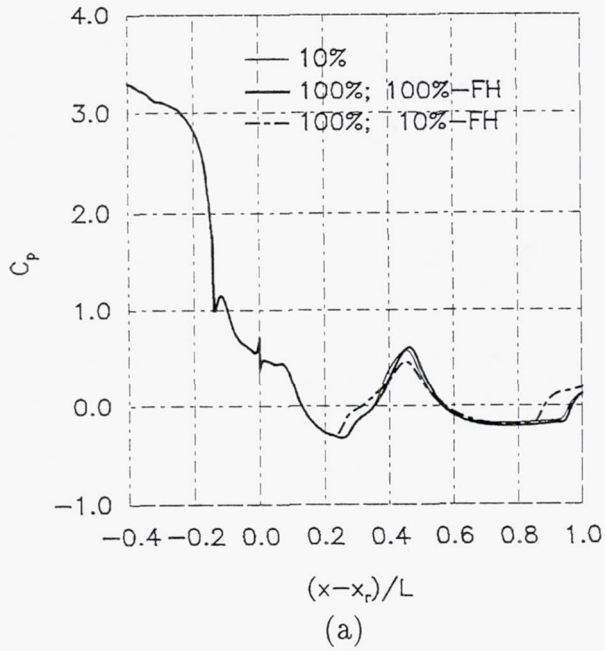Fig. 28. Scaling effect on the pressure coefficient on the expansion ramp. Results are presented for a 10% scale, full scale, and a full scale model with a 10% flameholder. (a) $M_\infty = 1.8$; (b) $M_\infty = 1.2$.

Fig. 29. Mach number contours for (a) 10% scale model, and (b) 100% scale model with a 10% scale flameholder. Part (c) shows a detail of the flow near the flameholder of part (b).

REPORT DOCUMENTATION PAGE

Public reporting burden for this collection of information is estimated to average 1 hour per response, including the time for reviewing instructions, searching existing data sources, gathering and maintaining the data needed, and completing and reviewing the collection of information. Send comments regarding this burden estimate or any other aspect of this collection of information, including suggestions for reducing this burden, to Washington Headquarters Services, Directorate for Information Operations and Reports, 1215 Jefferson Davis Highway, Suite 1204, Arlington, VA 22202-4302, and to the Office of Management and Budget, Paperwork Reduction Project (0704-0188), Washington, DC 20503.

1. AGENCY USE ONLY (Leave blank)	2. REPORT DATE April 1992	3. REPORT TYPE AND DATES COVERED Technical Memorandum

4. TITLE AND SUBTITLE

Computational Study of Single-Expansion-Ramp Nozzles With External Burning

5. FUNDING NUMBERS

WU–505–90–5R

6. AUTHOR(S)

Shaye Yungster, Charles J. Trefney

7. PERFORMING ORGANIZATION NAME(S) AND ADDRESS(ES)

National Aeronautics and Space Administration
Lewis Research Center
Cleveland, Ohio 44135–3191

8. PERFORMING ORGANIZATION REPORT NUMBER

E–8702

9. SPONSORING/MONITORING AGENCY NAME(S) AND ADDRESS(ES)

National Aeronautics and Space Administration
Washington, D.C. 20546–0001

10. SPONSORING/MONITORING AGENCY REPORT NUMBER

NASA TM–106550
ICOMP–94–5

11. SUPPLEMENTARY NOTES

Shaye Yungster, Institute for Computational Mechanics in Propulsion, Lewis Research Center (work funded under NASA Cooperative Agreement NCC3–233). Charles J. Trefny, NASA Lewis Research Center. ICOMP Program Director, Louis Povinelli, (216) 433–5818.

12a. DISTRIBUTION/AVAILABILITY STATEMENT

Unclassified-Unlimited
Subject Category 34

12b. DISTRIBUTION CODE

13. ABSTRACT (Maximum 200 words)

A computational investigation of the effects of external burning on the performance of single expansion ramp nozzles (SERN) operating at transonic speeds is presented. The study focuses on the effects of external heat addition and introduces a simplified injection and mixing model based on a control volume analysis. This simplified model permits parametric and scaling studies that would have been impossible to conduct with a detailed CFD analysis. The CFD model is validated by comparing the computed pressure distribution and thrust forces, for several nozzle configurations, with experimental data. Specific Impulse calculations are also presented which indicate that external burning performance can be superior to other methods of thrust augmentation at transonic speeds. The effects of injection fuel pressure and nozzle pressure ratio on the performance of SERN nozzles with external burning are described. The results show trends similar to those reported in the experimental study, and provide additional information that complements the experimental data, improving our understanding of external burning flowfields. A study of the effect of scale is also presented. The results indicate that combustion kinetics do not make the flowfield sensitive to scale.

14. SUBJECT TERMS

Transonic drag reduction; External burning

15. NUMBER OF PAGES
28

16. PRICE CODE
A03

17. SECURITY CLASSIFICATION OF REPORT Unclassified	18. SECURITY CLASSIFICATION OF THIS PAGE Unclassified	19. SECURITY CLASSIFICATION OF ABSTRACT Unclassified	20. LIMITATION OF ABSTRACT

NSN 7540-01-280-5500

Standard Form 298 (Rev. 2-89)
Prescribed by ANSI Std. Z39-18
298-102